

Reconfigurable asymmetrical broadband mid-infrared light filter design by materials informatics

Cite as: Appl. Phys. Lett. **126**, 101701 (2025); doi: [10.1063/5.0250763](https://doi.org/10.1063/5.0250763)

Submitted: 27 November 2024 · Accepted: 21 February 2025 ·

Published Online: 10 March 2025



View Online



Export Citation



CrossMark

Jiang Guo¹ and Junichiro Shiomi^{1,2,3,a)} 

AFFILIATIONS

¹Department of Mechanical Engineering, The University of Tokyo, 7-3-1 Hongo, Bunkyo, Tokyo 113-8656, Japan

²Institute of Engineering Innovation, The University of Tokyo, 7-3-1 Hongo, Bunkyo, Tokyo 113-8656, Japan

³RIKEN Center for Advanced Intelligence Project, 1-4-1 Nihombashi, Chuo-ku, Tokyo 103-0027, Japan

^{a)}Author to whom correspondence should be addressed: shiomi@photon.t.u-tokyo.ac.jp

ABSTRACT

A reconfigurable asymmetrical broadband mid-infrared light filter utilizing a vanadium dioxide (VO₂) triangular grating structure is designed by materials informatics. The design applies the unique phase-transition characteristics of VO₂ to facilitate asymmetrical light transmission, enhancing forward transmission via surface plasmon polaritons when VO₂ is metallic state at high temperatures. At lower temperatures, as VO₂ transitions to a dielectric state, no free electrons are available for excitation, resulting in a more symmetric transmission. The operational bandwidth or wavelength of the filter can be adjusted through geometric parameters of the triangular structures.

Published under an exclusive license by AIP Publishing. <https://doi.org/10.1063/5.0250763>

The mid-infrared (MIR) spectral range, which spans from 2 to 20 μm , is important for a wide range of applications, including chemical sensing,^{1–3} environmental monitoring,⁴ medical diagnostics,⁵ thermal imaging,⁶ and telecommunications.⁷ The development of compact, efficient, and tunable MIR optical components, such as filters, modulators, or isolators, remains challenging due to their limited tunability, narrow operational bandwidths, or large sizes.^{8–11} Asymmetric light transmission is a unique phenomenon in optical engineering that allows light to pass preferentially in one direction while being obstructed or reflected in the opposite direction, similar to the function of an optical diode or isolator.^{12,13} This unidirectional transmission capability is crucial for optical isolators, circulators, and other nonreciprocal devices to prevent undesirable feedback and improve the efficiency of optical systems.^{14–16} Asymmetric light transmission can be achieved by exploiting geometric asymmetries or material anisotropies in nanophotonic structures, enabling the manipulation of light paths based on the incidence direction.¹⁷ The concept of asymmetric light transmission has been extensively investigated based on advances in nanophononics, particularly through the use of metamaterials and plasmonic structures. These nanophotonic devices can be designed to support the constructive interference of optical modes in the forward direction while generating destructive interference or scattering in the reverse direction, resulting in effective asymmetric light transmission.^{18–24} For example, triangular metallic gratings have been shown to support asymmetric transmission by

enabling high-order diffraction modes in the forward direction and suppressing them in the reverse direction via a suitable geometric design.²⁵ Chiral metamaterials, which lack mirror symmetry, have similarly demonstrated asymmetric transmission via the selective rotation of incident-light polarization, rendering the transmission behavior dependent on the propagation direction.²⁶

There are many reported asymmetrical transmission filter designs. Xu *et al.*¹⁸ utilized the double grating to realize the narrow-band asymmetrical transmission for color filter. Lin *et al.*²⁵ employed triangle grating structures and realized asymmetrical transmission for both transverse magnetic (TM) and transverse electric (TE) polarization states near 1.55 μm . Tang *et al.*²⁷ applied the tapered-metal-grating structure and designed the broadband asymmetric transmission in the visible frequency range. Wong *et al.*²⁸ used the trapezoid silver grating to design the asymmetrical transmission device for radiative cooling in the mid-infrared light range. However, many existing asymmetric transmission devices are limited by their static nature and cannot adapt to changing environmental and operational conditions. The integration of phase-change materials, such as vanadium dioxide (VO₂), into optical structures is a promising solution for achieving dynamically tunable asymmetric transmission. VO₂ undergoes a reversible phase transition from an insulating to a metallic state near 68 °C, which significantly alters its optical properties.²⁴ This phase transition allows VO₂-based devices to modulate light transmission and reflection in real time, enabling the development of reconfigurable

optical components that can adapt to external stimuli.^{29–32} The tunability of VO₂ has been demonstrated in various optical applications. Kang *et al.*³¹ proposed to use Au/VO₂-based active metasurfaces for ultrafast optical modulation. Sun *et al.*³³ reported using 40-nm VO₂ metasurface to dynamically control thermal emission in the infrared range. Kocer *et al.*³⁴ applied VO₂ planar thin-film structure for the tunable broadband infrared absorber design. Kim *et al.*³⁵ used the VO₂ based switchable radiator for the spacecraft thermal control, however, operate as reciprocal systems without asymmetrical contrast. Thus, VO₂ is an ideal candidate for adaptive asymmetrical MIR optical systems.³⁶ In addition to material advances, materials informatics has enabled the development of efficient tools for optimizing the design of optical devices.^{37–40} Materials informatics employs data-driven approaches, including machine learning, to efficiently explore large material-parameter spaces, enabling the discovery of novel material combinations or configurations that exhibit optimal performance.^{41–46}

This Letter introduces a reconfigurable asymmetrical broadband MIR light filter based on a VO₂ triangular grating structure optimized through materials informatics. The design combines the phase-transition properties of VO₂ and the geometric asymmetry of the triangle grating, enabling the dynamic control of asymmetrical light transmission across a broad wavelength range of 5–16 μm .

A triangular VO₂ wire structure was used in this study. The optical response was simulated using the rigorous coupled-wave analysis

(RCWA) method using the open-source package S4.⁴⁷ RCWA, which is also known as the Fourier modal method, is an efficient numerical method for analyzing the diffraction efficiency of electromagnetic waves in periodic photonic structures. This method expands the electromagnetic fields and material properties in terms of the Fourier series, transforms Maxwell's electromagnetic equations into series-coupled differential equations, and solves these equations to obtain the electromagnetic-field distributions as well as each order of the reflection and transmission diffraction efficiencies.⁴⁸

In the RCWA simulation, the triangular VO₂ wire structure was modeled as a periodic grating along the x-direction and approximated by segmenting the triangle into multiple rectangular sections of equal height along the z-direction, as shown in Fig. 1(a). The benchmark triangular structure has a bottom length of 10 μm , a height of 10 μm , and a pitch size of 16 μm . The VO₂ is assumed to be in its metallic state, surrounded by air medium and illuminated by *p*-polarized light at normal incidence in the simulation model. The medium in both incident and transmission areas is set to be air in the simulation setup. However, it is possible to use practical substrate material instead. The VO₂ optical constant data were obtained from literature and then interpolated.⁴⁹ The VO₂ optical constants in its metallic and dielectric states are shown in Fig. 1(b). The dependence on the number of sliced rectangles, as shown in Fig. 1(c), indicates that 30 rectangles are sufficient for the simulation. Similarly, the dependence result on the

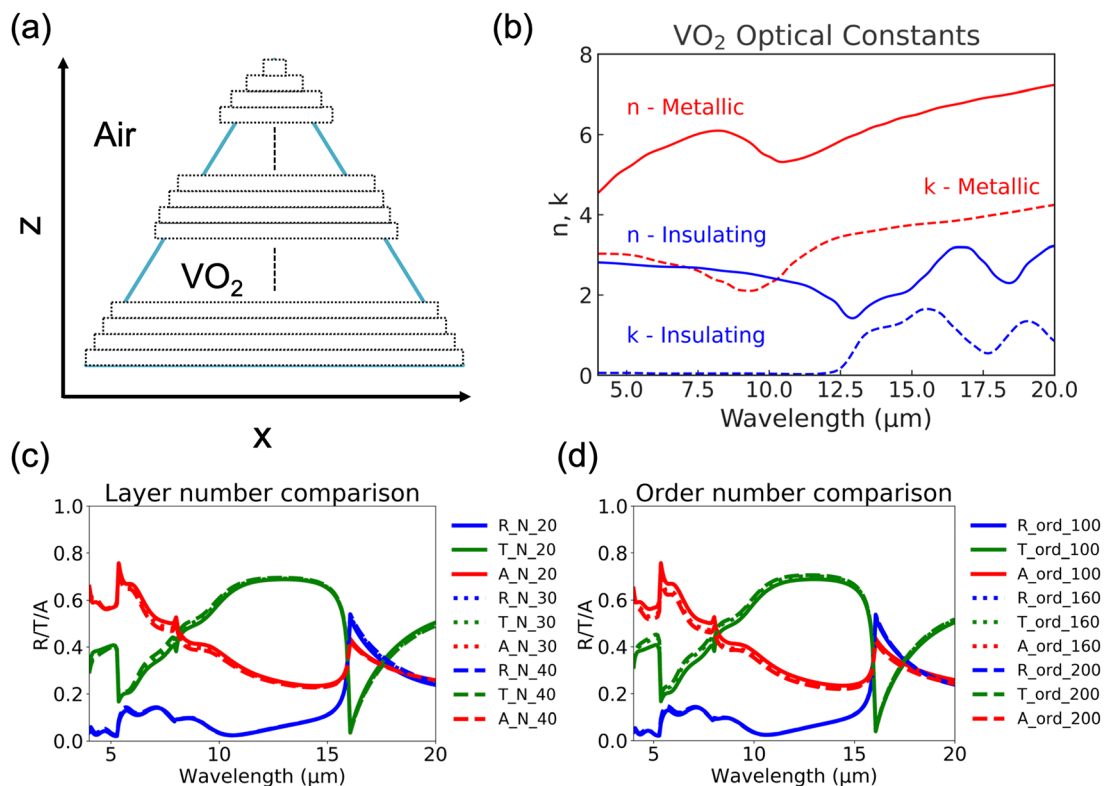


FIG. 1. (a) The computational model for benchmarking: The triangular VO₂ structure is periodic along the x-direction and discretized into rectangular plates of equal height along the z-direction. The bottom length, height, and pitch size of the triangle are 10, 10, and 16 μm , respectively. In the simulation model, VO₂ is in its metallic state, surrounded by air medium and illuminated normally by *p*-wave. (b) VO₂ optical constant data for the metallic and dielectric state. (c) Dependence of results on the number *N* of sliced rectangular plates with *N* = 20, 30 and 40. (d) Dependence of results on the number of harmonic-order in the simulation, with 100, 160 and 200 orders.

harmonic order, as shown in Fig. 1(d), reveals marginal differences in the outcomes for diffraction orders exceeding 160. Given the exponential increase in computational cost, the number of rectangles and the harmonic order for the subsequent RCWA simulations were set to 30 and 160, respectively, to reduce the computational load.

For the materials informatics optimization, the Bayesian optimization approach was used to optimize the parameters of the triangular cross section shape of the VO₂ wire. The optimization was performed using a Bayesian-optimization open-source package.⁵⁰ The optimization parameters included the triangular bottom length, height, and pitch size, each ranging from 1 to 20 μm, and with the constraint wherein the pitch size must exceed the bottom length. A figure-of-merit (FOM) was specified to maximize the transmission contrast between forward and backward transmissions within 5–16 μm, which is the range where most room-temperature thermal-radiation fluxes occur. The FOM is expressed as follows:

$$\text{FOM} = \frac{1}{\lambda_2 - \lambda_1} \int_{\lambda_1}^{\lambda_2} (t_F - t_B) d\lambda, \quad (1)$$

where λ_1 and λ_2 are 5 and 16 μm, respectively, and t_F and t_B are the forward and backward transmission properties at temperature above 68 °C when VO₂ is in the metallic state, respectively. Theoretically, forward and backward transmissions do not differ significantly at temperatures below 68 °C when VO₂ is in the dielectric state.

The Bayesian optimization can efficiently explore the parameter space by iteratively refining predictions using a Gaussian Process (GP) regression model. The GP model was constructed with a Matern kernel,⁵⁰ a generalization of the Radial Basis Function (RBF) kernel, allowing flexibility in controlling the smoothness of the modeled function. The kernel is defined as

$$k(x_i, x_j) = \frac{1}{\Gamma(\nu)2^{\nu-1}} \left(\frac{\sqrt{2\nu}}{l} d(x_i, x_j) \right)^\nu K_\nu \left(\frac{\sqrt{2\nu}}{l} d(x_i, x_j) \right), \quad (2)$$

in which the hyperparameter ν is used to control the smoothness of the resulting function. If ν is infinite large, kernel becomes equivalent

to the RBF kernel. d is the Euclidean distance between two points. Γ is the gamma function and K is the modified Bessel function. The Matern kernel's adaptability ensures a robust representation of the objective function across the parameter space. To balance exploration of uncharted regions and exploitation of promising areas, we utilized the Expected Improvement (EI) acquisition function. The EI function is expressed as

$$\text{EI}(x) = (f_{\text{best}} - \mu(x)) \Phi \left(\frac{f_{\text{best}} - \mu(x)}{\sigma(x)} \right) + \sigma(x) \phi \left(\frac{f_{\text{best}} - \mu(x)}{\sigma(x)} \right), \quad (3)$$

where $\mu(x)$ and $\sigma(x)$ represent the predicted mean and standard deviation at x , respectively. Φ and ϕ are the cumulative distribution function (CDF) and probability density function (PDF) of the standard normal distribution. The first term encourages exploitation by favoring regions near the predicted best values, while the second term promotes exploration in regions with high uncertainty. By maximizing the EI function, the next sampling point is determined, effectively guiding the optimization process. The Bayesian optimization process begins with an initial sampling of the design parameter space, followed by iterative updates of the GP model as new observations are incorporated. At each step, the EI acquisition function is optimized to identify the next design parameters for evaluation. This iterative process continues until convergence criteria are met, such as a minimal improvement in the objective function or reaching a predefined number of iterations.

Ten rounds of independent Bayesian optimization were conducted, each with a different random seed, and 50 initial data points were used to train the Gaussian process regression model. As depicted in Fig. 2(a), almost all rounds of the optimization converged rapidly to the maximum FOM after a few hundred iterations, thereby demonstrating the high efficiency of the Bayesian-optimization approach. The triangular bottom, height, and pitch size corresponding to FOM exceeding 0.2 were obtained and analyzed, as shown in Fig. 2(b). The distribution of the bottom and pitch sizes was more confined compared to the broader height distribution, with the pitch size fixed at approximately 16 μm. This closely aligns with the Wood anomalies cutoff wavelength,²⁵ which can be calculated as follows:

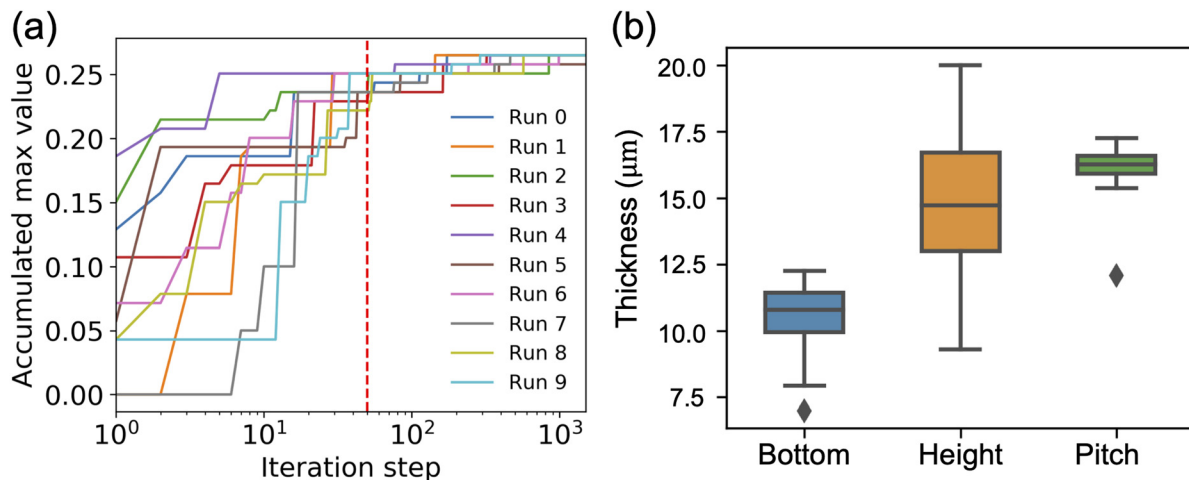


FIG. 2. (a) Bayesian-optimization results obtained using different random seeds for 10 independent runs. (b) Size-distribution analysis of FOM values exceeding 0.2. Boxes span the interquartile range, lines inside the boxes denote medians, and diamonds indicate outliers.

$$\lambda = \sqrt{\epsilon}P, \quad (4)$$

where ϵ is the dielectric constant of the substrate medium and P is the pitch size. Because the substrate was set as vacuum, the cutoff diffraction wavelength was exactly the pitch size. Furthermore, one of the optimized VO₂ triangular wire structures was selected for simulation and demonstration, with its bottom length, height, and pitch being [10.28, 9.64, and 16.02] μm . The simulation was performed under normal incidence with p -polarized wave.

The simulation results for the optimized triangular VO₂ wire structure's optical response revealed a significant transmission contrast between forward and backward modes within the 5–16 μm range at temperatures above 68 °C, where VO₂ is in the metallic state, as shown in Fig. 3. For wavelengths above 16 μm , no difference was observed in terms of the optical response, including reflection (R), transmission (T), and absorption (A), between the forward and backward modes, due to the absence of diffraction waves in this range. When VO₂ was in the dielectric state at temperatures below 68 °C, its optical properties did not support the excitation of surface plasmon polaritons (SPPs), and the optical response between the forward and backward modes showed minimal difference, as the SPPs resonance effects were not activated under these conditions. Comparing forward mode transmission for temperatures above and below 68 °C, a higher level of transmission was observed in the 5–16 μm range for temperatures above 68 °C. By contrast, the backward-mode transmission showed minimal variation

between temperatures above and below 68 °C within the same wavelength range. This dynamic, temperature-dependent behavior of VO₂ allows for adjustable transmission filtering, making it a good fit for tunable photonic applications. The backward mode remains stable across temperature changes, while the forward mode adjusts based on the temperature, showing its adaptability. These features make VO₂ useful for devices that need to change their optical properties in response to environmental conditions, such as smart windows and sensors. This adaptability is especially valuable in practical settings where conditions vary.

For better understanding of the findings, a comparative analysis of the transmission contrast and related performance metrics from this study and prior works was conducted. Table I highlights key parameters, including forward and backward transmission magnitudes, tunability property, operational wavelength, and structural configurations.

To investigate the underlying physical mechanisms, the electromagnetic-field distribution was analyzed at selected wavelengths of 5.36, 12.5, and 16.0 μm . For comparison, the forward and backward electromagnetic-field distribution, including the magnetic and Poynting fields, are plotted at the top and bottom of the figures, respectively, as discussed in the following part.

The observed asymmetric transmission in the VO₂ triangular cross section wire structure can be explained based on SPPs excitation and the interplay between high-order diffraction channels.^{21,25}

At 5.36 μm , the metallic VO₂ supports SPP modes localized at the metal–dielectric interface. The SPPs' current flowing along the

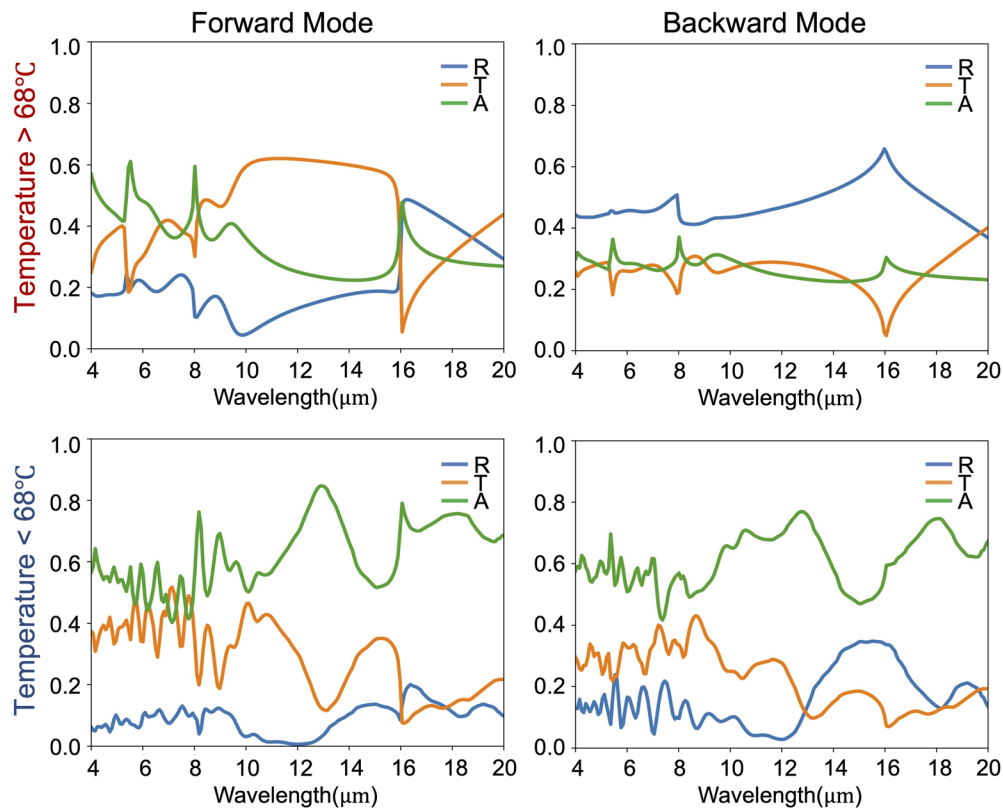


FIG. 3. Forward and backward optical responses for optimized triangular-shaped VO₂ wire structure, shown for temperature above 68 °C in metallic state (top row) and temperature below 68 °C in dielectric state (bottom row). Blue line represents reflection (R), orange line represents transmission (T), and green line represents absorption (A).

TABLE I. Comparison of asymmetrical transmission filters.

Structure	Wavelength	Forward	Backward	Tunability	Reference
Triangle grating (Ag)	1.55 μm	0.83	0.31	No	25
Trapezoid grating (Ag)	600 nm	0.95	0.35	No	27
Trapezoid grating (Ag)	8.5 μm	0.91	0.12	No	28
Trapezoid grating (Al)	540 nm	0.62	0.14	No	19
Trapezoid grating (Al)	640 nm	0.31	0.04	No	51
Double grating (Au)	1.20 μm	0.72	0.12	No	52
Double grating (Ag/SiO ₂)	1.25 μm	0.96	0.15	No	53
Double grating (Cr/Ag/ZnO)	532 nm	0.98	0.05	No	18
Graphene/h-BN grating	38.13 THz	0.79	0.05	Yes	54
Metamaterial (VO ₂ /Au)	3.57 THz	0.62	0.04	Yes	55
Photonic crystal (Ag)	0.62 μm	0.96	0.12	No	56
This work	12.5 μm	0.69	0.28	Yes	

surface of the triangle in the forward direction facilitates efficient energy transfer and guidance of light through the structure with less scattering, as depicted from the magnetic-field plots in Fig. 4, where the hotspots at the triangle edges indicate localized energy transfer, and the arrows indicate the electric current flow. The forward incidence allows high diffraction orders to be efficiently coupled into the transmitted modes, thus resulting in a strong forward transmission. At 12.0 μm , a combination of fundamental and low-order SPPs was observed at the metal-dielectric interface. The magnetic-field plots at this wavelength show nodes and antinodes, indicating a combination of different diffraction modes, which contribute to the forward transmission. Furthermore, the electric-field distribution profiles in Fig. 5 show clear evidence of both fundamental and higher-order SPPs' excitations at 5.36 and 12.5 μm , respectively. The strong electric-field hotspots localized along the edges and nodes of the triangular structures confirm the efficient coupling of surface plasmon modes. This coupling facilitates the confinement and guided transfer of energy, which are crucial for producing the observed asymmetric transmission effects. At 16.0 μm , where the wavelength matches the pitch size of the structure, the transmission behavior is attributed to the Wood anomalies, where higher-order diffraction modes transition to evanescent as their diffraction angles reach the grazing condition. This results in the suppression of higher-order modes and a redistribution of optical

energy, concentrating it primarily in the zeroth order. By contrast, when light was incident from the reverse direction for all selected wavelengths, the SPPs excitation condition was disrupted owing to phase mismatch between the incident wave and structure. Consequently, strong scattering and reflection occurred because the SPPs current was not efficiently supported in the reverse direction, and the high diffraction orders were switched from transmission to reflection mode.

The Poynting-field distribution shown in Fig. 6 illustrates the energy flow at different wavelengths. At 5.36 μm , the forward incidence exhibited strong SPPs excitation, with localized field spots appearing at the interface between the metallic VO₂ and the surrounding medium, particularly near the edges of the triangular structure, indicating efficient energy transfer. At 12.5 μm , the forward mode showed a more uniform distribution of the Poynting field across the triangle's surface, with nodes and antinodes that reflect interference effects from fundamental and low-order diffraction modes. The energy flow remained directional, thereby supporting efficient forward transmission. At 16.0 μm , the forward-model Poynting fields were more diffused and flowed in parallel at the bottom area, which indicates less transmission and more reflection. By contrast, for reverse incidence, the Poynting field showed scattered energy in the incident direction, which resulted in significant reflection. The absence of SPPs excitation

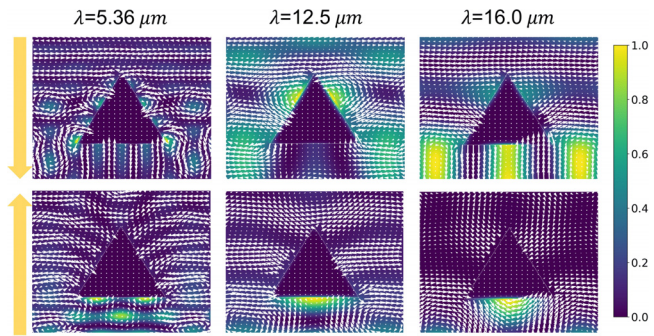


FIG. 4. Magnetic-field distribution at wavelengths of 5.36, 12.5, and 16.0 μm for forward light incidence (top row) and backward light incidence (bottom row). The arrow on the left shows light incidence direction, while field arrows indicate electric-field flow.

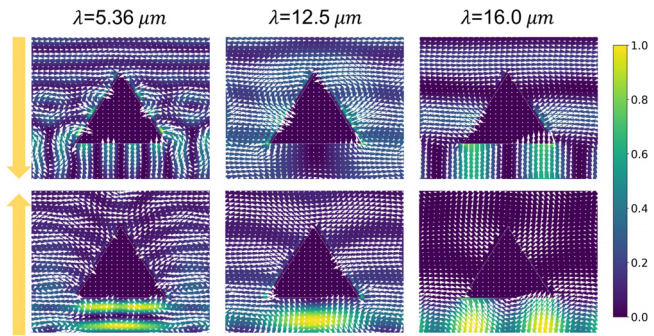


FIG. 5. Electric-field distribution at wavelengths of 5.36, 12.5, and 16.0 μm for forward light incidence (top row) and backward light incidence (bottom row). The arrow on the left shows light incidence direction, while field arrows indicate electric-field flow.

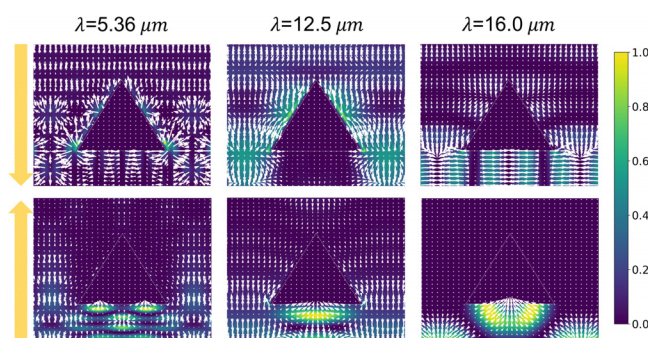


FIG. 6. Poynting-field distribution at wavelengths of 5.36, 12.5, and 16.0 μm for forward light incidence (top row) and backward light incidence (bottom row). The arrow on the left shows light incidence direction, while field arrows indicate electric-field flow.

in the reverse direction was caused by phase mismatch, which resulted in most of the energy being reflected instead of transmitted.

In summary, a reconfigurable asymmetrical broadband MIR optical filter was designed based on materials informatics. The asymmetrical transmission was due to the asymmetrical SPPs resonance and the interplay between the diffraction modes. The phase transition property of VO_2 enables the transmission filter to dynamically switch from asymmetrical to symmetrical transmission with temperature changes. The operational bandwidth or wavelength of the reconfigurable filter can be easily adjusted by modifying the size parameters based on materials informatics. Thus, the filter is suitable for various applications, such as radiative cooling, thermophotovoltaic, and energy-efficient asymmetrical window filters.

This study was partially supported by CREST (Grant No. JPMJCR21O2) of the Japan Science and Technology Agency.

AUTHOR DECLARATIONS

Conflict of Interest

The authors have no conflicts to disclose.

Author Contributions

Jiang Guo: Conceptualization (lead); Data curation (lead); Formal analysis (lead); Methodology (lead); Writing – original draft (lead).
Junichiro Shiomi: Funding acquisition (lead); Supervision (lead); Writing – review & editing (lead).

DATA AVAILABILITY

The data that support the findings of this study are available from the corresponding author upon reasonable request.

REFERENCES

- K. O. Ash, "Chemical sensing: An approach to biological molecular mechanisms using difference spectroscopy," *Science* **162**(3852), 452–454 (1968).
- H. Zhu, C. Xu, D.-W. Wang, V. V. Yakovlev, and D. Zhang, "Enhanced chemical sensing with multiorder coherent Raman scattering spectroscopic dephasing," *Anal. Chem.* **94**(23), 8409–8415 (2022).
- S. Svanberg, "Chemical sensing with laser spectroscopy," *Sens. Actuators, B* **33**(1), 1–4 (1996).
- J. A. Hodgeson, W. A. McClenny, and P. L. Hanst, "Air pollution monitoring by advanced spectroscopic techniques," *Science* **182**(4109), 248–258 (1973).
- F. Vigo, A. Tozzi, M. Disler, A. Gisi, V. Kavvadias, and T. Kavvadias, "Vibrational spectroscopy in urine samples as a medical tool: Review and overview on the current state-of-the-art," *Diagnostics* **13**(1), 27 (2022).
- B. Kateb, V. Yamamoto, C. Yu, W. Grundfest, and J. P. Gruen, "Infrared thermal imaging: A review of the literature and case report," *NeuroImage* **47**, T154–T162 (2009).
- K. Zou, K. Pang, H. Song, J. Fan, Z. Zhao, H. Song, R. Zhang, H. Zhou, A. Minoofar, C. Liu, X. Su, N. Hu, A. McClung, M. Torfeh, A. Arbabi, M. Tur, and A. E. Willner, "High-capacity free-space optical communications using wavelength- and mode-division-multiplexing in the mid-infrared region," *Nat. Commun.* **13**(1), 7662 (2022).
- A. Y. Hwang, H. S. Stokowski, T. Park, M. Jankowski, T. P. McKenna, C. Langrock, J. Mishra, V. Ansari, M. M. Fejer, and A. H. Safavi-Naeini, "Mid-infrared spectroscopy with a broadly tunable thin-film lithium niobate optical parametric oscillator," *Optica* **10**(11), 1535–1542 (2023).
- T. Xu, Y. Dong, Q. Zhong, S. Zheng, Y. Qiu, X. Zhao, L. Jia, C. Lee, and T. Hu, "Mid-infrared integrated electro-optic modulators: A review," *Nanophotonics* **12**(19), 3683–3706 (2023).
- W. Zhou, D. Wu, R. McClintock, S. Slivken, and M. Razeghi, "High performance monolithic, broadly tunable mid-infrared quantum cascade lasers," *Optica* **4**(10), 1228–1231 (2017).
- T. Huang, X. Zhao, S. Zeng, A. Crunteanu, P. P. Shum, and N. Yu, "Planar nonlinear metasurface optics and their applications," *Rep. Prog. Phys.* **83**(12), 126101 (2020).
- Z. Yu and S. Fan, "Complete optical isolation created by indirect interband photonic transitions," *Nat. Photonics* **3**(2), 91–94 (2009).
- D. Jalas, A. Petrov, M. Eich, W. Freude, S. Fan, Z. Yu, R. Baets, M. Popović, A. Melloni, J. D. Joannopoulos, M. Vanwolleghem, C. R. Doerr, and H. Renner, "What is—and what is not—an optical isolator," *Nat. Photonics* **7**(8), 579–582 (2013).
- A. D. White, G. H. Ahn, K. V. Gasse, K. Y. Yang, L. Chang, J. E. Bowers, and J. Vucković, "Integrated passive nonlinear optical isolators," *Nat. Photonics* **17**(2), 143–149 (2023).
- H. Tian, J. Liu, A. Siddharth, R. N. Wang, T. Blésin, J. He, T. J. Kippenberg, and S. A. Bhave, "Magnetic-free silicon nitride integrated optical isolator," *Nat. Photonics* **15**(11), 828–836 (2021).
- M. Yu, R. Cheng, C. Reimer, L. He, K. Luke, E. Puma, L. Shao, A. Shams-Ansari, X. Ren, H. R. Grant, L. Johansson, M. Zhang, and M. Lončar, "Integrated electro-optic isolator on thin-film lithium niobate," *Nat. Photonics* **17**(8), 666–671 (2023).
- A. S. Ansari, A. K. Iyer, and B. Gholipour, "Asymmetric transmission in nanophotonics," *Nanophotonics* **12**(14), 2639–2667 (2023).
- T. Xu and H. J. Lezec, "Visible-frequency asymmetric transmission devices incorporating a hyperbolic metamaterial," *Nat. Commun.* **5**(1), 4141 (2014).
- A. Ozer, H. Kocer, and H. Kurt, "Broadband and polarization-independent asymmetric transmission of visible light through a three-dimensional trapezoidal metallic metasurface," *J. Opt. Soc. Am. B* **35**(9), 2111–2117 (2018).
- B. Chen, S. Yang, J. Chen, J. Wu, K. Chen, W. Li, Y. Tan, Z. Wang, H. Qiu, K. Fan, C. Zhang, H. Wang, Y. Feng, Y. He, B. Jin, X. Wu, J. Chen, and P. Wu, "Directional terahertz holography with thermally active Janus metasurface," *Light* **12**(1), 136 (2023).
- Y. Ling, L. Huang, W. Hong, T. Liu, Y. Sun, J. Luan, and G. Yuan, "Asymmetric optical transmission based on unidirectional excitation of surface plasmon polaritons in gradient metasurface," *Opt. Express* **25**(12), 13648–13658 (2017).
- B. Khalichi, A. Ghobadi, A. K. Osgouei, and E. Ozbay, "Diode like high-contrast asymmetric transmission of linearly polarized waves based on plasmon-tunneling effect coupling to electromagnetic radiation modes," *J. Phys. D* **54**(36), 365102 (2021).
- A. Abudula and Z. Sun, "Asymmetric optical transmission of a metallic grating-incorporated Fabry-Pérot cavity," *J. Phys. D* **55**(19), 195101 (2022).
- S. S. Kruk, L. Wang, B. Sain, Z. Dong, J. Yang, T. Zentgraf, and Y. Kivshar, "Asymmetric parametric generation of images with nonlinear dielectric metasurfaces," *Nat. Photonics* **16**(8), 561–565 (2022).
- Y. Lin, "Asymmetric light transmission based on a 1D triangular metal grating," *J. Opt. Soc. Am. B* **37**(5), 1428–1433 (2020).

- ²⁶M. I. Khan, B. Hu, A. Amanat, N. Ullah, M. J. I. Khan, and A. R. Khalid, "Efficient asymmetric transmission for wide incidence angles using bi-layered chiral metasurface," *J. Phys. D* **53**(30), 305004 (2020).
- ²⁷B. Tang, Z. Li, Z. Liu, F. Callewaert, and K. Aydin, "Broadband asymmetric light transmission through tapered metallic gratings at visible frequencies," *Sci. Rep.* **6**(1), 39166 (2016).
- ²⁸R. Y. M. Wong, C. Y. Tso, C. Y. H. Chao, B. Huang, and M. P. Wan, "Ultra-broadband asymmetric transmission metallic gratings for subtropical passive daytime radiative cooling," *Sol. Energy Mater. Sol. Cells* **186**, 330–339 (2018).
- ²⁹M. M. Qazilbash, M. Brehm, B.-G. Chae, P.-C. Ho, G. O. Andreev, B.-J. Kim, S. J. Yun, A. V. Balatsky, M. B. Maple, F. Keilmann, H.-T. Kim, and D. N. Basov, "Mott transition in VO₂ revealed by infrared spectroscopy and nano-imaging," *Science* **318**(5857), 1750–1753 (2007).
- ³⁰H. Guan, F. Ren, S. Liang, J. Gu, C. Geng, H. Wei, S. Dou, J. Zhao, and Y. Li, "Ultra-high transmission broadband tunable VO₂ optical limiter," *Laser Photonics Rev.* **17**(4), 2200653 (2023).
- ³¹T. Kang, Z. Ma, J. Qin, Z. Peng, W. Yang, T. Huang, S. Xian, S. Xia, W. Yan, Y. Yang, Z. Sheng, J. Shen, C. Li, L. Deng, and L. Bi, "Large-scale, power-efficient Au/VO₂ active metasurfaces for ultrafast optical modulation," *Nanophotonics* **10**(2), 909–918 (2020).
- ³²S. Zhao, L. Li, J. Zhu, M. Liu, T. Zhou, C. Zhou, Z. Lin, J. Li, B. Sun, Y. Lu, and C. Zou, "Self-excited free-standing VO₂ film for infrared optical limiter," *Laser Photonics Rev.* **18**(10), 2400426 (2024).
- ³³K. Sun, W. Xiao, C. Wheeler, M. Simeoni, A. Urbani, M. Gaspari, S. Mengali, C. H. (de Groot, and O. L. Muskens, "VO₂ metasurface smart thermal emitter with high visual transparency for passive radiative cooling regulation in space and terrestrial applications," *Nanophotonics* **11**(17), 4101–4114 (2022).
- ³⁴H. Kocer, S. Butun, E. Palacios, Z. Liu, S. Tongay, D. Fu, K. Wang, J. Wu, and K. Aydin, "Intensity tunable infrared broadband absorbers based on VO₂ phase transition using planar layered thin films," *Sci. Rep.* **5**(1), 13384 (2015).
- ³⁵H. Kim, K. Cheung, R. C. Y. Auyeung, D. E. Wilson, K. M. Charipar, A. Piqué, and N. A. Charipar, "VO₂-based switchable radiator for spacecraft thermal control," *Sci. Rep.* **9**(1), 11329 (2019).
- ³⁶K. Liu, S. Lee, S. Yang, O. Delaire, and J. Wu, "Recent progresses on physics and applications of vanadium dioxide," *Mater. Today* **21**(8), 875–896 (2018).
- ³⁷S. Ju and J. Shiomi, "Materials informatics for heat transfer: Recent progresses and perspectives," *Nanoscale Microscale Thermophys. Eng.* **23**(2), 157–172 (2019).
- ³⁸S. Ju, S. Shimizu, and J. Shiomi, "Designing thermal functional materials by coupling thermal transport calculations and machine learning," *J. Appl. Phys.* **128**(16), 161102 (2020).
- ³⁹K. T. Butler, D. W. Davies, H. Cartwright, O. Isayev, and A. Walsh, "Machine learning for molecular and materials science," *Nature* **559**(7715), 547–555 (2018).
- ⁴⁰S. Ramakrishna, T.-Y. Zhang, W.-C. Lu, Q. Qian, J. S. C. Low, J. H. R. Yune, D. Z. L. Tan, S. Bressan, S. Sanvito, and S. R. Kalidindi, "Materials informatics," *J. Intell. Manuf.* **30**(6), 2307–2326 (2019).
- ⁴¹A. Sakurai, K. Yada, T. Simomura, S. Ju, M. Kashiwagi, H. Okada, T. Nagao, K. Tsuda, and J. Shiomi, "Ultrathin-band wavelength-selective thermal emission with aperiodic multilayered metamaterials designed by Bayesian optimization," *ACS Cent. Sci.* **5**(2), 319–326 (2019).
- ⁴²D. Zhu, J. Guo, G. Yu, C. Y. Zhao, H. Wang, and S. Ju, "Designing thermal radiation metamaterials via a hybrid adversarial autoencoder and Bayesian optimization," *Opt. Lett.* **47**(14), 3395–3398 (2022).
- ⁴³Q. Wang, Z. Huang, J. Li, G.-Y. Huang, D. Wang, H. Zhang, J. Guo, M. Ding, J. Chen, Z. Zhang, Z. Rui, W. Shang, J.-Y. Xu, J. Zhang, J. Shiomi, T. Fu, T. Deng, S. G. Johnson, H. Xu, and K. Cui, "Module-level polaritonic thermophotovoltaic emitters via hierarchical sequential learning," *Nano Lett.* **23**(4), 1144–1151 (2023).
- ⁴⁴W. Zhang, B. Wang, and C. Zhao, "Selective thermophotovoltaic emitter with aperiodic multilayer structures designed by machine learning," *ACS Appl. Energy Mater.* **4**(2), 2004–2013 (2021).
- ⁴⁵J.-W. Cho, Y.-J. Lee, J.-H. Kim, R. Hu, E. Lee, and S.-K. Kim, "Directional radiative cooling via exceptional epsilon-based microcavities," *ACS Nano* **17**(11), 10442–10451 (2023).
- ⁴⁶J. Guo, S. Ju, Y. Lee, A. A. Gunay, and J. Shiomi, "Photonic design for color compatible radiative cooling accelerated by materials informatics," *Int. J. Heat Mass Transfer* **195**, 123193 (2022).
- ⁴⁷V. Liu and S. Fan, "S4: A free electromagnetic solver for layered periodic structures," *Comput. Phys. Commun.* **183**(10), 2233–2244 (2012).
- ⁴⁸M. G. Moharam and T. K. Gaylord, "Rigorous coupled-wave analysis of planar-grating diffraction," *J. Opt. Soc. Am.* **71**(7), 811–818 (1981).
- ⁴⁹A. M. Morsy, M. T. Barako, V. Jankovic, V. D. Wheeler, M. W. Knight, G. T. Papadakis, L. A. Sweatlock, P. W. C. Hon, and M. L. Povinelli, "Experimental demonstration of dynamic thermal regulation using vanadium dioxide thin films," *Sci. Rep.* **10**(1), 13964 (2020).
- ⁵⁰"bayesian-optimization/Bayesian Optimization" (2024).
- ⁵¹N. Yilmaz, A. Ozer, F. T. Bagci, O. O. Kilic, T. Yildirim, A. Ozdemir, H. Kocer, and H. Kurt, "Optical sensing device through monitoring cut-off wavelength of asymmetric transmission," in *20th International Conference on Transparent Optical Networks (ICTON)*, 2018.
- ⁵²Y. Ren, C. Jiang, and B. Tang, "Asymmetric transmission in bilayer chiral metasurfaces for both linearly and circularly polarized waves," *J. Opt. Soc. Am. B* **37**(11), 3379–3385 (2020).
- ⁵³S. Li, L. Huang, Y. Ling, W. Liu, C. Ba, and H. Li, "High-performance asymmetric optical transmission based on coupled complementary subwavelength gratings," *Sci. Rep.* **9**(1), 17117 (2019).
- ⁵⁴H. Hajian, A. Ghobadi, A. E. Serebryannikov, B. Butun, G. A. E. Vandenbosch, and E. Ozbay, "Tunable infrared asymmetric light transmission and absorption via graphene-hBN metamaterials," *J. Appl. Phys.* **126**(19), 193102 (2019).
- ⁵⁵Z. Liu, T. Zhou, G. Jin, J. Su, and B. Tang, "Switchable asymmetric transmission with broadband polarization conversion in vanadium dioxide-assisted terahertz metamaterials," *Phys. Chem. Chem. Phys.* **26**(2), 1017–1022 (2024).
- ⁵⁶R. Zhu, X. Wu, Y. Hou, G. Zheng, J. Zhu, and F. Gao, "Broadband asymmetric light transmission at metal/dielectric composite grating," *Sci. Rep.* **8**(1), 999 (2018).